Bioorganic Chemistry 180 (2026) 110154

Contents lists available at ScienceDirect

Bioorganic Chemistry

journal homepage: www.elsevier.com/locate/bioorg

Insight into the reactivity and antitumoral potential of allyl rhodanine derivatives: Azomethine ylide cycloadditions, molecular docking, and SAR studies

Redouane Er-raqioui [a,b,c], José A.S. Cavaleiro [b], M. Amparo F. Faustino [b], Filipe A. Almeida Paz [d], Maurizio Viale [e], Fabrizio Loiacono [f], El Mostapha Rakib [a,c,*], Maria da Graça P.M.S. Neves [b], Florbela Pereira [g,*], Nuno M.M. Moura [b,*]

[a] Laboratory of Molecular Chemistry, Materials and Catalysis, Faculty of Sciences and Technics, Sultan Moulay Slimane University, Beni-Mellal, BP 523, Morocco
[b] LAQV-REQUIMTE, Department of Chemistry, University of Aveiro, 3810-193 Aveiro, Portugal
[c] Higher School of Technology, Sultan Moulay Slimane University, BP 336 Fkih Ben Salah, Morocco
[d] CICECO – Aveiro Institute of Materials, Department of Chemistry, University of Aveiro, 3810-193 Aveiro, Portugal
[e] U.O. Bioterapie, IRCCS Azienda Ospedale Policlinico San Martino, L.go R. Benzi, 10, 16132 Genova, Italy
[f] U.O. Immunologia, IRCCS Azienda Ospedale Policlinico San Martino, L.go R. Benzi, 10, 16132 Genova, Italy
[g] LAQV-REQUIMTE, Chemistry Department, NOVA School of Science and Technology, NOVA FCT, Lisbon Campus, 2829-516 Caparica, Portugal

ARTICLE INFO

Keywords:
Rhodanine
[3 + 2] cycloaddition
Spiro compounds
Antitumoral
Molecular docking
Molecular dynamics
ADMET

ABSTRACT

In this work, a series of *N*-allyl-5-arylidene-rhodanine derivatives was prepared and their reactivity evaluated as dipolarophiles in 1,3-dipolar cycloaddition reactions. Cycloadducts of series **5** were obtained using sarcosine and 5-nitroisatin as precursors, while reactions with sarcosine and 2-pyridinecarboxaldehyde afforded new 2-pyridyl-substituted spiro derivatives (series **7**). All compounds from both series were fully characterized and screened for their *in vitro* anticancer activity against the following five human cancer cell lines: A2780 (ovarian carcinoma), A549 (lung adenocarcinoma), MDA-MB-231 (breast carcinoma), NCI-N592 (small-cell lung cancer), and A431 (epidermoid carcinoma). Several derivatives exhibited pharmacologically relevant IC_{50} values, with compounds **5b** and **7b** demonstrating noteworthy antiproliferative activity in A549 cells, a standard model for non-small cell lung carcinoma. The apoptotic potential of the most active compounds was further confirmed by Annexin V/PI assays in A549 cells. Using baicalein as a reference inhibitor, both compound series were also subjected to molecular docking studies targeting the human enzyme 15-lipoxygenase-2 (*h*15-LOX-2), implicated in cancer-related pathways. In general, a consistent trend was observed between the antiproliferative activity of the compounds and their predicted inhibition of *h*15-LOX-2, as inferred from docking analysis of 28 structures, including the 10 final allyl rhodanine-based compounds and their required precursors. To further evaluate target engagement, molecular dynamics (MD) simulations were performed for the most active derivatives, providing mechanistic insight into binding-pocket rigidification and conformational stability. In addition, *in silico* ADMET predictions were carried out to assess the developability profile of the lead candidates. The integrated chemical synthesis, biological evaluation, and computational modeling provided key insights into the reactivity, bioactivity, and structure–activity relationships of the synthesized compounds.

1. Introduction

The heterocycle scaffold rhodanine, also known as 2-thioxo-4-thiazolidinone, represents a highly versatile structural motif widely employed in the synthesis of derivatives exhibiting diverse biological and pharmacological activities (Fig. 1) [1]. Reported activities include antidiabetic [2], antiviral [3], anti-inflammatory [4], antimicrobial [3,5], antimalarial [6], antifungal [7], anti-HIV [8], antidepressant [9], and anticancer properties [3,10–13].

Among the various strategies available for synthesizing new rhodanine derivatives, 1,3-dipolar cycloaddition (or [3 + 2] cycloaddition) reactions stand out as a powerful and versatile approach for

* Corresponding authors.
E-mail addresses: E.RAKIB@usms.ma (E.M. Rakib), florbela.pereira@fct.unl.pt (F. Pereira), nmoura@ua.pt (N.M.M. Moura).

https://doi.org/10.1016/j.bioorg.2026.110154
Received 5 November 2025; Received in revised form 15 May 2026; Accepted 22 June 2026
Available online 24 June 2026

incorporating five-membered heterocycles into their core structure [14,15]. In these reactions, rhodanine derivatives typically serve as the unsaturated 2π-electron component (dipolarophile), while azomethine ylides are usually used as the three-atom component (1,3-dipoles) [16–20]. Among these, azomethine ylides are particularly valuable for synthesizing spirooxindoles and pyrrolidinylpyridine-type derivatives. For example, spirooxindoles can be synthesized from azomethine ylides generated *in situ* from sarcosine and isatin through reaction with various dipolarophiles [21]. These compounds are of significant interest due to their potential therapeutic activities (Fig. 1), such as spirooxindoles exhibit anticancer, antiviral and antibacterial properties [22–26], underscoring their importance in medicinal chemistry.

Given the importance of lipid metabolism and regulated cell death in cancer, many anticancer compounds exert their effects by targeting enzymes involved in these processes. Among these, lipoxygenases (LOXs) have attracted significant attention due to their critical role in the metabolism of polyunsaturated fatty acids and modulation of cell death pathways. These enzymes, which contain non-heme iron, are responsible for the regio- and stereospecific incorporation of molecular oxygen into polyunsaturated fatty acids that possess at least two isolated *cis* double bonds, such as arachidonic acid (AA) [27,28]. This catalytic process produces optically active hydroperoxide derivatives. In humans, six lipoxygenase (LOX) isoforms have been characterized: 5-lipoxygenase (5-LOX), 12*R*-lipoxygenase, 12*S*-lipoxygenase, 15-lipoxygenase-1 (15-LOX-1), 15-lipoxygenase-2 (15-LOX-2), and epidermal lipoxygenase-3. These enzymes are classified according to the position at which they insert oxygen into the substrate [27,28]. For instance, 15-LOX converts the common substrate AA to 15-hydroperoxyeicosatetraenoic acid (15-HPETE) by oxygenating at carbon 13, whereas 5-LOX targets carbon 7 to yield 5-HPETE. Alterations in the levels of 15-LOX-2 expression have been reported in human renal and breast cancers [29]. Furthermore, recent studies indicate that *h*15-LOX-2, along with other LOX isoforms, may participate in ferroptosis, an iron-dependent cell death mechanism associated with lipid peroxidation [30].

Following the work of Murugan et al. [17], who first reported the reactivity of 5-arylidene-rhodanine derivatives with azomethine ylides generated from isatin and sarcosine, and considering the well-established anticancer potential of rhodanine-based frameworks, we aimed to evaluate both the impact of an *N*-allyl substituent on the reactivity of 5-arylidene-rhodanine derivatives of type **3** (*vide infra* Scheme 2) with azomethine ylides and the anticancer activity of the obtained cycloadducts. In the initial studies, the azomethine ylide generated from sarcosine and 5-nitroisatin was used as a model system. This strategy was then extended to the synthesis of new pyridyl-spiro derivatives using the azomethine ylide generated from 2-pyridinecarboxaldehyde and sarcosine (*vide infra* Scheme 3). The selection of this pyridine-based aldehyde was motivated by the synthetic versatility and biological relevance of the pyridyl scaffold in bioactive compounds [31–35].

All derivatives from each series were further evaluated for their anticancer activity against five human cancer cell lines: ovarian carcinoma A2780, lung adenocarcinoma A549, breast carcinoma MDA-MB-231, small-cell lung cancer NCI-N592, and epidermoid carcinoma A431, to provide a comprehensive evaluation of their biological potential. The apoptotic activity of the most promising derivatives was further investigated by Annexin V/PI staining in A549 cells. In light of the observed anticancer activity, molecular docking studies, including baicalein as a reference inhibitor, were conducted to explore potential molecular targets underlying their bioactivity. In the context of cancer-related pathways, particular attention has been directed towards the lipoxygenase enzymes (LOXs), especially *h*15-LOX-2, owing to their well-established roles in lipid peroxidation, inflammation, and tumorigenesis. The most active derivatives were further analyzed by molecular dynamics (MD) simulations to assess binding stability and conformational behavior at the *h*15-LOX-2 active site, and their physicochemical, pharmacokinetic, and toxicity (ADMET) properties were predicted *in silico* to support a developability assessment.

2. Results and discussion

2.1. Synthesis of dispiro-indole-pyrrolidine-rhodanine conjugates 5

The reactivity of rhodanine scaffolds **3** (Scheme 1), bearing allyl functionalities, was first investigated using the azomethine ylide generated from sarcosine and 5-nitroisatin (Scheme 2). This dipole was selected based on previous studies involving analogous rhodanine derivatives lacking substitution on the nitrogen atom of the 2-thioxothiazolidin-4-one ring [17]. This comparative approach enabled a more

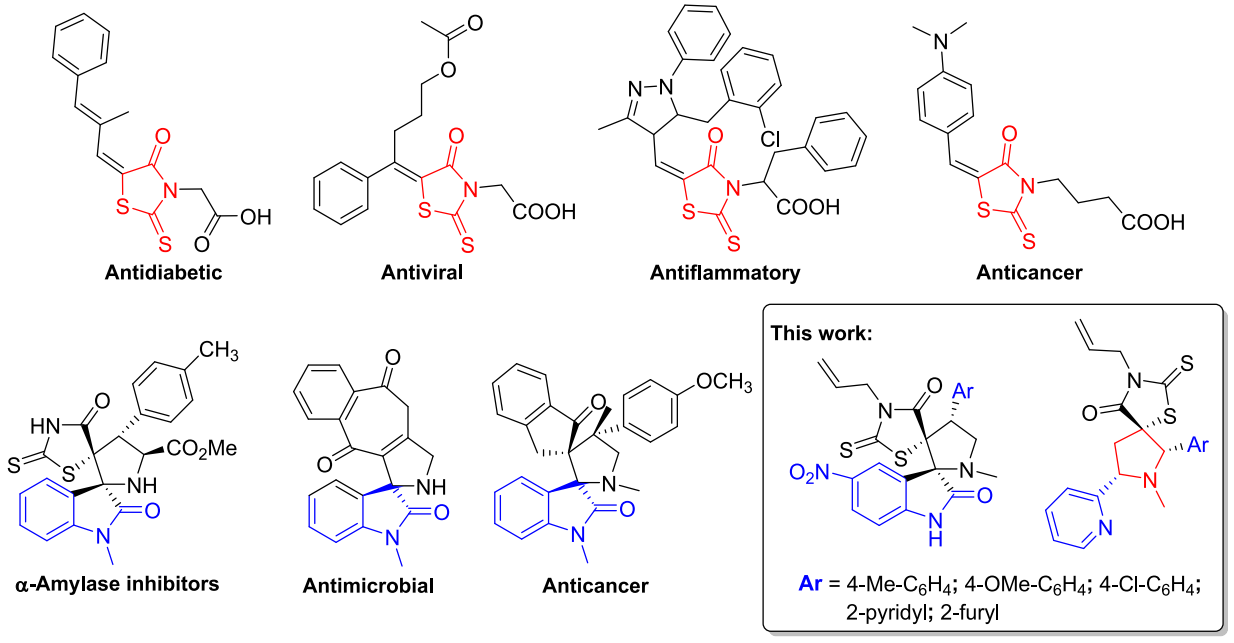

Fig. 1. Examples of bioactive compounds based on rhodanine and spirooxindole, heterocyclic scaffolds and the structures of the spiro compounds designed in the scope of this work.

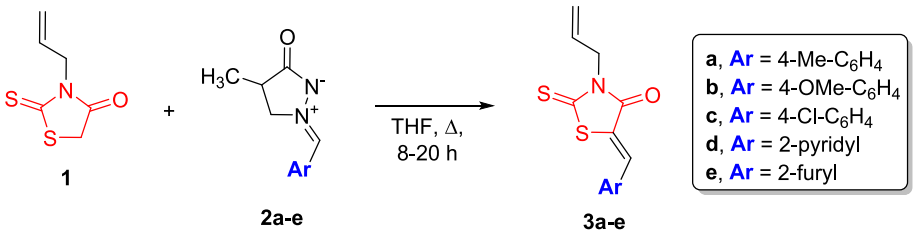

Scheme 1. Synthetic access to the initial scaffolds of type **3.**

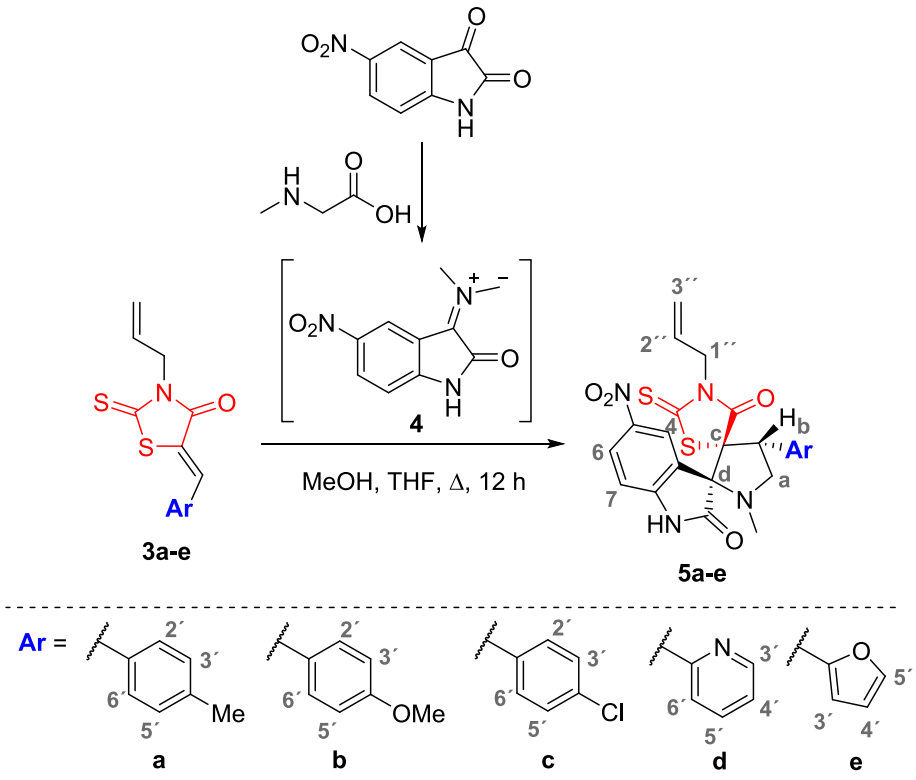

Scheme 2. Products obtained in the reaction of rhodanine scaffolds **3a-e** with the azomethine ylide generated from 5-nitroisatin and sarcosine.

effective evaluation of the impact of the newly introduced functional group. These derivatives were synthesized by following the approach previously described by El Ajlaoui *et al.*, which involves the reaction of 3-allylrhodanine with the appropriate 2-aryl/heteroarylidene-4-methyl-5-oxopyrazolidinium ylides [36].

The reactions with the azomethine ylide generated from 5-nitroisatin (1 equiv) and sarcosine (1 equiv) were performed in the presence of derivatives **3a–e** and were carried out in a refluxing mixture of tetrahydrofuran (THF) and methanol (1,1). The reaction progress was monitored by TLC, and complete consumption of the starting reagents was observed after approximately 12 h. The solvents were evaporated, and the crude products were purified by column chromatography using a chloroform-petroleum ether mixture. After crystallization, the pure main products **5a–e** were isolated with yields ranging from 50% to 66%.

The molecular structures of dispiro-indole-pyrrolidine-rhodanine conjugates **5a–e** were clearly established through comprehensive spectroscopic analysis, including 1D and 2D NMR, UV–Vis, FTIR and mass spectrometry. Detailed data are provided in the Supporting Information (see Experimental Section and Figs. S1–S30). The observed regioselectivity aligns with previous results obtained by other groups working with similar rhodanine scaffolds that lacked the *N*-allyl functionality [20,36,37]. It is worth noting that derivatives **5a–e** were isolated as a pair of enantiomers with *R,R,R* and *S,S,S* configurations.

For instance, in the ^{1}H NMR spectrum of compound **5c**, the resonance of the benzylic proton (H_b) appears as a doublet of doublets at δ 4.61 ppm (J = 9.7, 7.9 Hz), while the diastereotopic protons H_a of the pyrrolidine ring appear as a triplet at δ 4.04 ppm (J = 9.7 Hz) and doublet of doublets at δ 3.67 ppm (J = 9.7, 7.9 Hz). These data unequivocally confirm the regioselectivity observed in the reaction. The presence of multiplets, at δ 5.48–5.36 and δ 4.99–4.88 ppm due to the *N*-allyl protons H-2″ and H-3″ respectively and of the two doublet of doublets at δ 4.47 ppm and δ 4.37 ppm attributed to the CH_2 protons of the same unit confirm the absence of reaction involving the double bond of the allyl unit. The aromatic protons of the *p*-chlorophenyl unit appear as a multiplet at *ca.* δ 7.3 ppm, while a broad singlet at δ 8.03 ppm is attributed to the *N*H proton of the oxindole group.

In the ^{13}C NMR spectrum of cycloadduct **5c**, key peaks are observed at δ 196.9 ppm, assigned to the resonances of the thiocarbonyl, while the peaks at δ 176.6 ppm and δ 176.4 ppm are attributed to the resonances of the two cyclic amide carbonyl carbons. Signals at δ 73.2 ppm and δ 79.2 ppm are assigned to the resonance of the spiro carbons (C_c and C_d respectively). The ^{1}H and ^{13}C NMR profiles of the other adducts are similar to that of **5c,** with the main differences arising from the nature of the different aryl/heteroaryl substituents. Absorption spectra of derivatives **5a–e** show a similar profile with a strong absorption band ranging from 302 to 307 nm and a less intense band at around 450 nm

(Fig. S30).

The structure of the new derivative **5c** was further confirmed by ESI (+) mass spectrometry, which showed a peak at *m/z* 515.0 corresponding to the expected $[M + H]^+$ molecular ion. For the other adducts, the molecular structure was also confirmed by the presence of the expected protonated molecular ion. It should be noted that attempts to obtain products from further reaction at the allyl bond using an excess of azomethine ylide, generated from 5-nitroisatin and sarcosine, were unsuccessful.

2.2. Synthesis of 2-pyridyl-substituted spiro–pyrrolidine–rhodanine conjugates 7

Given that pyridyl-based heterocycles can be easily synthesized by exploring the reactivity of various dipolarophiles with azomethine ylides derived from sarcosine and 2-pyridinecarboxaldehyde [38] and building on the adducts obtained in previous studies, we decided to explore 5-arylidene allylrhodanine scaffolds to develop new pyridyl-spiropyrrolidine–rhodanines.

The cycloaddition reactions with the scaffolds **3a–e** were carried out in refluxing toluene in the presence of pyridine-2-carbaldehyde and sarcosine. After 12 h, TLC analysis confirmed the consumption of the reactants and the formation of a major new product (Scheme 3). The solvent was then removed under reduced pressure, and the residue was recrystallized from methanol to afford pure products **7a–e** in yields ranging from 64% to 77%.

The structures of the spiropyrrolidine-rhodanine conjugates **7a–e** were unambiguously established by comprehensive spectroscopic analysis, including 1D and 2D NMR, UV–Vis, FTIR, as well as mass spectrometry. Full characterization data are available in the Supporting Information (see Experimental Section and Figs. S31–S59).

In this adduct series, the formation of the regioisomers **7a–e** was confirmed by the ^{1}H NMR analysis. For instance, in **7a** (Scheme 3), the proton H_b from the pyrrolidine unit appears in the multiplet at δ 4.56–4.46 ppm together with the protons H-1″, while the diastereotopic protons H_a appear as a doublet of doublets at δ 3.78 ppm (J = 10.1, 8.2 Hz) and as a triplet at δ 3.23 ppm (J = 10.1 Hz); proton H_c appears as a singlet at δ 4.67 ppm. In the aliphatic region the singlets at δ 2.54 ppm and δ 2.33 ppm were assigned to the CH_3 linked to the aromatic ring and to the nitrogen from the pyrrolidine unit. The presence of a multiplet at δ 5.83–5.75 ppm due to the resonance of H-2″ and of a triplet at δ 5.23 ppm due to the H-3″ confirmed the presence of the allylic chain. As before, the peaks at 199.5 ppm and 175.7 ppm in the ^{13}C NMR spectrum of cycloadducts **7a–e** confirmed the absence of reaction at the thiocarbonyl and carbonyl carbons. The carbon peaks at around δ 75 ppm were assigned to the resonance of the spiro carbon of each compound. NMR spectra of the other adducts followed a similar profile. All compounds of the spiropyrrolidine-rhodanine conjugates series **7a–e** exhibited similar UV–Vis spectra with an absorption band maximum at around 305 nm (Fig. S59). Both series of compounds (**5a–e** and **7a–e**) exhibited high structural stability in DMF solutions. For each derivative, the presence of a peak in its mass spectrum corresponding to the expected protonated molecular ion $[M + H]^+$ confirmed its molecular formula. Altogether, this validated the successful synthesis of this new series of 2-pyridyl derivatives.

2.3. Crystallographic studies

Crystallographic studies of compound **7c** reveal that the molecular units present in the crystal structure correspond to a racemic mixture between the (*S*,*S*,*S*) and (*R*,*R*,*R*) isomers (see Fig. 2 with the chiral centers being represented by an asterisk). Though the synthesis could lead, in theory, to eight possible isomers, a powder X-ray diffraction pattern of the bulk material of **7c** (Fig. S60) clearly shows that the determined crystal structure corresponds to the whole of the obtained compound from the synthetic procedure described in the experimental section.

With the absence of specific groups capable of strong hydrogen

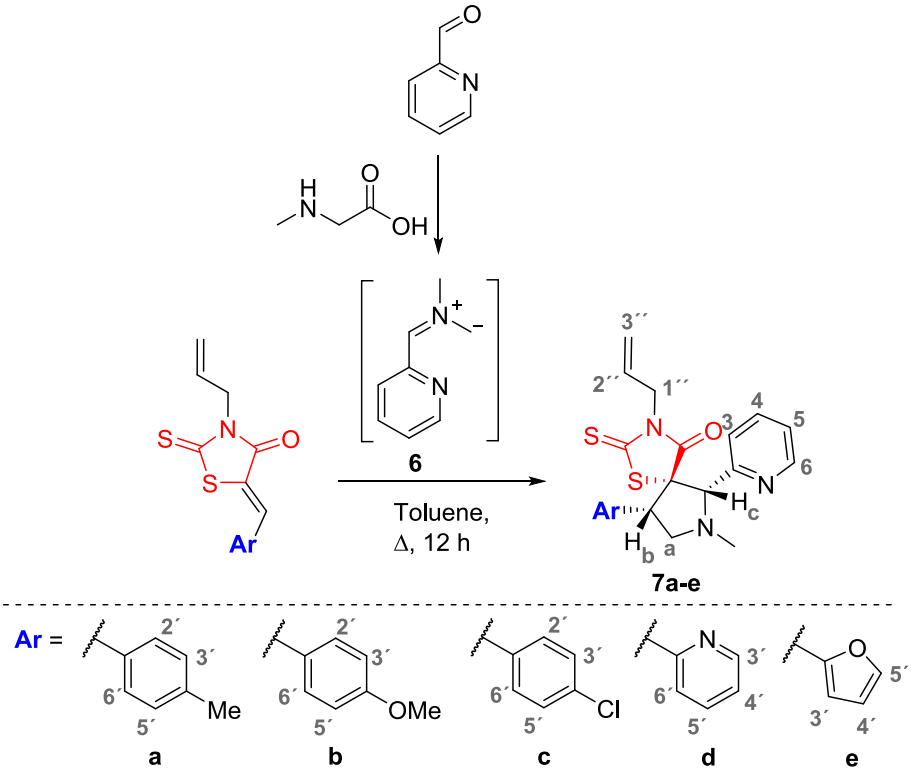

Scheme 3. Structures of products **7a–e** obtained in the reaction of rhodanine scaffolds with the azomethine ylide obtained *in situ* from pyridine-2-carbaldehyde and sarcosine.

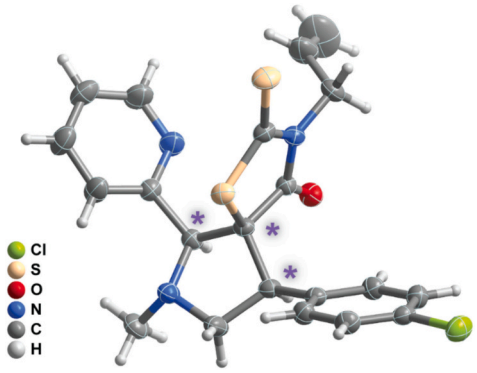

Fig. 2. Schematic representation of the molecular unit present in compound **7c**. Asymmetric centers are depicted by an asterisk. Please note: the configuration shown is the (*S,S,S*) enantiomer; the crystal structure also contains the (*R,R,R*) enantiomer. Non-hydrogen atoms are represented as thermal ellipsoids drawn at the 30% probability level and hydrogen atoms as small spheres with arbitrary radii.

bonding interactions, the crystal packing of **7c** in the solid state is mostly mediated by the need to effectively fill the available space, with only a handful of weak supramolecular interactions (not shown).

2.4. Antiproliferative activity of compounds 5a–e and 7a–e in human cancer cell lines and apoptosis

The antiproliferative activity of the ten compounds **5a–e** and **7a–e** was evaluated by using the MTT assay on five human cancer cell lines A2780 (ovarian carcinoma), A549 (lung adenocarcinoma), MDA-MB-231 (breast carcinoma), NCI-N592 (small-cell lung cancer), and A431 (epidermoid carcinoma). The assessment followed a two-step protocol. In the first step, each compound was tested at a single concentration of 30 μM, considered here as the upper limit for a pharmacologically significant IC_{50}. The second step, using a concentration range (serial dilutions), was applied only to those compounds that, at 30 μM, were able to reduce cell proliferation to values equal to or lower than 50% of the untreated controls and were active in at least two cancer cell lines.

In the initial screening, only 6 out of 10 compounds (**5a**–**5e** and **7b**) met the selection criterion, showing percent cell proliferation at 30 μM lower than 50% of controls (Table 1). In particular, **5a**–**e** and **7b** showed significant antiproliferative activity against A2780 ovarian carcinoma cells. Compounds **5a**, **5b**, **5d**, **5e** and **7b** were also active against A549 lung adenocarcinoma cells, while **5b** and **5c** significantly inhibited proliferation of MDA-MB-231 breast cancer cells. Finally, compound **5c** was active against NCI-N592 small-cell lung cancer cells, while compounds **5b–5d** appeared to be active against A431 epidermoid carcinoma cells, although their IC_{50} values were borderline with respect to the arbitrary threshold defined above (Table 1).

To confirm these preliminary results and determine the IC_{50} values of compounds **5a–e** and **7b**, these compounds were further tested using the same cancer cell lines exposed to a concentration range (see Fig. S61).

In general, the results obtained in this second step of antiproliferative analysis (Table 2) corroborated the initial observations. Pharmacologically significant IC_{50} values were obtained for compounds **5a** and **7b** against A2780 and A549 cells; for **5b** against A2780, A549, and MDA-MB-231 cells; for **5c** against A2780, MDA-MB-231, and NCI-N592 cells; for **5d** in A2780 cells with a borderline IC_{50} value in A549; and for **5e** in A2780 and A549 cells, with a borderline IC_{50} value in MDA-MB-231 cells. Notably, also in this case, none of the tested compounds showed significant activity against the A431 cell line, and only compounds **5b**–**d**, exhibited IC_{50} values close to the arbitrary 30 μM threshold.

The results obtained in A549 with **5a**, **5b** and **7b**, namely the latter two, are particularly noteworthy, as they suggest relevant antiproliferative activity against a cell line that is a typical cell model of non-small cell lung cancer (NSCLC). Indeed, these neoplasms represent about 85% of all lung cancer and are one of the leading causes of cancer-related deaths worldwide, primarily as a consequence of smoking [39]. Similarly, the activity observed for compound **5c** in NCI-N592 small-cell lung cancer cells is of interest and warrants further investigation, given the characteristic initial responsiveness of this tumor type to treatment followed by frequent relapse after variable periods.

In a series of parallel experiments aimed at assessing a possible selectivity index (SI) towards cancer cells, peripheral blood mononuclear cells (PBMNCs), stimulated with 1% PHA and IL-2, were treated with the active compounds. The SI was calculated as the ratio between the IC_{50} obtained in PBMNCs and the pharmacologically relevant IC_{50}

Table 1
Percent proliferation of A2780, A549, MDA-MB-231, NCI-N592, and A431 cells treated with 30 μM of each compound **5a–e** and **7a–e**. Values are expressed as percentage of untreated control (100%) ± standard deviation.

Compd	Cell line				
	A2780	A549	MDA-MB-231	NCI-N592	A431
5a	24.2 ± 2.3[a] < 0.001[b]	37.7 ± 2.9 < 0.01	55.3 ± 2.3	53.3 ± 9.7	53.2 ± 6.3
5b	4.6 ± 0.6 < 0.001	11.7 ± 1.7 < 0.01	22.0 ± 6.1 < 0.01	53.4 ± 1.0	43.3 ± 4.9
5c	1.8 ± 0.8 < 0.001	63.2 ± 11.8	6.3 ± 2.5 < 0.001	32.2 ± 8.1 < 0.05	48.0 ± 4.5
5d	23.5 ± 5.7 < 0.01	40.5 ± 5.6 < 0.05	53.2 ± 3.0	55.4 ± 2.8	49.7 ± 7.9
5e	30.5 ± 6.7 < 0.02	39.6 ± 7.7	52.7 ± 3.8	98.6 ± 9.7	88.9 ± 0.7
7a	39.1 ± 1.6 < 0.001	64.6 ± 2.0	85.5 ± 12.3	65.7 ± 13.5	66.0 ± 6.6
7b	14.2 ± 2.7 < 0.001	20.8 ± 2.5 < 0.001	51.5 ± 3.7	50.4 ± 5.6	53.0 ± 5.5
7c	30.3 ± 3.8 < 0.01	57.4 ± 3.2	76.6 ± 8.0	77.3 ± 11.9	66.8 ± 10.2
7d	42.3 ± 3.4 < 0.05	73.2 ± 10.5	71.7 ± 5.6	ND	ND
7e	38.0 ± 4.5 < 0.02	67.9 ± 4.1	78.4 ± 5.7	80.9 ± 13.8	73.2 ± 6.4

[a] Numbers express the percent proliferation at 30 μM concentration of each compound compared to untreated controls (100%). Values significantly lower than 50% indicate possible IC_{50} values lower than 30 μM. [b] *P*-values were obtained by the one-sample *t*-test (reference value: 50%). ND – Not determined.

Table 2
Evaluation of IC_{50} values (μM) of the active spiropyrrolidine-rhodanine compounds **5a–e** and **7b** against A2780, A549, MDA-MB-231, NCI-N592, and A431 tumor cell lines, and against PBMNCs as a normal-cell reference.

Compd	Cell line					PBMNC
	A2780	A549	MDA-MB-231	NCI-N592	A431	
5a	11.4 ± 2.3 <0.001[a]	22.9 ± 4.3 <0.05	> 30	>30	>30	15.4 ± 4.0
5b	20.8 ± 6.0	10.1 ± 2.4	20.3 ± 2.8	>30	27.0 ± 4.5[b] NS	53 ± 1.9
5c	19.8 ± 3.3	> 30	17.4 ± 5.8	17.9 ± 2.9 <0.01	28.6 ± 2.8[b] NS	90 ± 6.2
5d	21.0 ± 3.3	29.1 ± 5.2[b]	> 30	>30	26.4 ± 11.5[b] NS	83 ± 4.9
5e	16.6 ± 4.6	24.6 ± 6.1	31.8 ± 2.4[a]	>30	>30	139 ± 1.3
7b	20.8 ± 5.3	12.8 ± 1.1	> 30	>30	>30	51 ± 2.3

[a] *P* values were obtained by the one-sample t-test (reference value: 30 μM). [b] Borderline value. NS – Not statistically significant ($p > 0.05$)

(< 30 μM) obtained in the cancer cell lines for each compound. The results obtained (Table 2) indicate SI values ranging from 3.3 to 8.4 for our compounds, with the exception of **5a**, which exhibited a marked inhibitory effect on cell proliferation across all PBMNC preparations tested. While this finding indicates a low selectivity index, it also opens the possibility of further investigating this compound, particularly in leukemic cells or in bone marrow blasts derived from leukaemia patients cultured in semisolid media, to evaluate its potential anti-leukemic activity.

To further characterize the cytotoxic potential of our lead compounds, we investigated the apoptotic effects of compounds **5a**, **5b**, and **7b** in A549 cells, where these molecules demonstrated significant biological activity. The results revealed that all tested compounds induced necrosis and apoptosis in both a concentration- and time-dependent manner, although not always in a strictly statistically significant manner. Among the evaluated derivatives, compound **5a** exhibited the highest apoptotic activity at pharmacologically relevant concentrations corresponding to the IC_{50} and IC_{75} values (Table 3 and Fig. S62).

2.5. Molecular docking

Considering the role of 15-LOX-2 in cancer promotion, as stated in the Introduction, it can be hypothesized that 15-LOX inhibitors may be considered promising chemotherapeutic agents. To explore this possibility, molecular docking studies were performed to elucidate the binding interactions of the ten newly synthesized allyl spiropyrrolidine-rhodanine-based derivatives **5a–e** and **7a–e** and their precursors, together with a docking control ligand ((hydroxyethyloxy)tri(ethyloxy) octane), the natural substrate arachidonic acid (AA) and the reference inhibitor baicalein, against the human 15-LOX-2 (*h*15-LOX-2) enzyme (PDB ID: 4NRE) [40]. Baicalein was selected as the reference compound due to its well-documented inhibitory activity against human lipoxygenases including *h*15-LOX-2, with a reported IC_{50} value of 38 μM [41]. Furthermore, it has demonstrated cytotoxic activity against several human cancer cell lines, with reported IC_{50} values of 46.23 μM (A2780) [42], 20 μM (A549) [43], and 44 μM (MDA-MB-231) [44]. The compounds tested included i) the starting allyl rhodanine **1**; ii) the five 2-aryl/heteroarylidene-4-methyl-5-oxopyrazolidinium ylides derivatives **2a–e** and the corresponding 3-allylrhodanine key precursors **3a–e**; iii) the azomethine ylide **4** and the resulting dispiropyrrolidine derivatives **5a–e** obtained from its reaction with compounds **3**; iv) the azomethine ylide **6** and the resulting 5-arylidene allylrhodanine derivatives (**7a–e**) obtained from its reaction with compounds **3**. The results from molecular docking simulations performed using AutoDock Vina software against the *h*15-LOX-2 enzyme are summarized in Table S1 of the Supplementary Data. Fig. 3 displays the best-docked pose of the docking control ((hydroxyethyloxy)tri(ethyloxy)octane) (**A**), of the substrate AA (**B**) and of the baicalein (**C**) on the *h*15-LOX-2 enzyme obtained using AutoDock Vina.

Similar binding poses were observed for the docking control ligand and AA, as shown in Fig. 3. Both ligands exhibited hydrophobic interactions with the catalytic residues Phe365, Leu420, and Val603, in agreement with the findings reported by Viviani et al. [45]. In contrast, a slightly different binding mode was observed for the reference compound baicalein, which exhibited hydrophobic interaction only with the catalytic residue Leu420. To validate the docking protocol, the co-crystallized ligand in PDB ID 4NRE was re-docked. PyMOL was used to align the protein backbones and to superimpose the docked and crystallographic ligand poses. The resulting root-mean-square deviation (RMSD) was 1.031 Å, indicating good agreement. A flexible molecular docking study using AutoDock Vina was performed to virtually screen the allyl rhodanine-based derivatives of both series **5** and **7** and their precursors to identify the most favorable binding interactions. The predicted binding affinities (AutoDock Vina scores, expressed in kcal/mol), obtained within the defined search space coordinates, are summarized in Table 4 for the top derivatives **5a–e** and **7a–e**, the docking control ligand ((hydroxyethyloxy)tri(ethyloxy)octane), AA and the reference compound baicalein.

As shown in Table 4, the most promising allyl rhodanine-based derivatives are those exhibiting the most favorable Vina scores. Notably, four derivatives from series **5**, namely **5a**, **5c**, **5b**, and **5e**, demonstrated docking scores equal to or lower than −7.9 kcal/mol (specifically −8.6, −8.4, −8.3, and − 7.9 kcal/mol, respectively). In contrast, none of the five derivatives from series **7** exhibited scores equal to or below −7.9 kcal/mol. Fig. 4 shows the four most probable lead-like *h*15-LOX-2 inhibitor poses, including **5a**, **5b**, **5c** and **5e**.

The four derivatives of the **5** series have similar binding poses, with all derivatives displaying two hydrogen-bond interactions between the 5-nitroindolin-2-one moiety and the Gln425 residue, as illustrated in Table 4 and Fig. 4. As shown in Fig. 5, derivative **5a** and all allyl spirorhodanine-based derivatives and their precursors exhibit different binding poses to the docking control ligand and AA. In contrast, these compounds exhibited binding poses highly similar to that of the reference compound, baicalein, as illustrated in Table 4 and Figs. 4 and 5. Notably, a hydrogen bond interaction with the Gln425 residue was observed for the derivatives of series **5** (except for derivative **5d**) and baicalein. Additionally, hydrophobic interactions were identified between certain derivatives (**5a** and **5c**), as well as baicalein, and the catalytic residues Leu420 and Ala606.

2.6. Molecular dynamics (MD) simulations

Molecular dynamics (MD) simulations performed with OpenMM [46–48] were used to investigate the stability, conformational behavior, and interaction persistence of the *h*15-LOX-2–ligand complexes selected as top candidates from molecular docking and biological evaluation. These simulations were carried out for the four allyl rhodanine-based derivatives (**5a–c** and **7b**) as well as for the reference inhibitor

Table 3
Evaluation of apoptosis by the annexin-V/PI test in A549 cells exposed to the IC_{50} and IC_{75} concentrations of active compounds.

Incubation Time	IC_{50}									
	Control		5a		5b		7b		7a (30 μM)	
	Necr[a]	Apo[b]	Necr	Apo	Necr	Apo	Necr	Apo	Necr	Apo
24 h	9.2 ± 3.5	7.6 ± 0.6	10.0 ± 2.0	6.0 ± 0.5	6.9 ± 0.2	6.4 ± 0.9	6.4 ± 0.3	5.9 ± 0.7	11.8 ± 1.8	6.4 ± 1.6
48 h	7.0 ± 3.9	5.4 ± 3.5	18.1 ± 5.0	8.0 ± 1.1	15.5 ± 5.2	4.5 ± 1.3	7.1 ± 3.1	5.2 ± 1.7	16.9 ± 4.6	6.3 ± 3.5
p value[c]			<0.05						<0.05	
Incubation Time	IC_{75} Control		5a		5b		7b			
	Necr	Apo	Necr	Apo	Necr	Apo	Necr	Apo		
24 h	9.2 ± 3.5	7.6 ± 0.6	11.8 ± 0.8	9.3 ± 0.5	10.0 ± 0.8	13.2 ± 1.0	16.4 ± 6.5	9.8 ± 1.3		
48 h	7.0 ± 3.9	5.4 ± 3.5	11.0 ± 7.0	34.5 ± 5.2	30.3 ± 3.9	18.5 ± 2.9	21.5 ± 5.2	11.5 ± 3.8		
p value				<0.01	<0.01	<0.01	<0.02			

Necr - stands for necrosis. Apo - stands for apoptosis. [a] - the numbers express the percentage of necrotic cells. [b] - the numbers express the percentage of apoptotic cells as the sum of early and late apoptotic cells. c - P-values were obtained by the student's *t*-test, as compared to control.

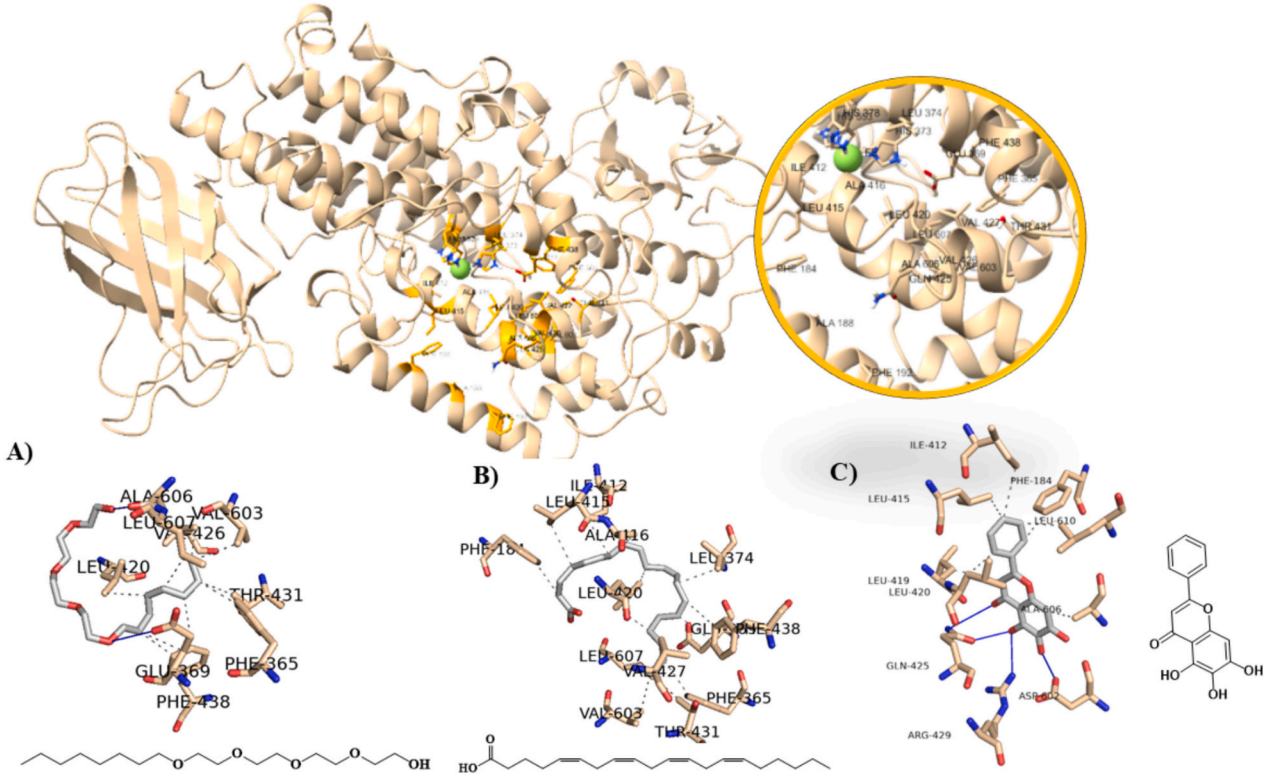

Fig. 3. Schematic representations of *h*15-LOX-2 overall structure and the active site's cavity, which is highlighted in orange. The catalytic iron is represented by a green sphere. The residues that coordinate Fe^{3+} (His-373, His-378, His-553) and the residues of the active site's cavity are also shown. The interaction profile of the best-docked pose for **A**) the docking control ligand ((hydroxyethyloxy)tri(ethyloxy)octane), for **B**) the substrate (AA) and for **C**) baicalein against the *h*15-LOX-2 enzyme. The hydrophobic interactions are represented by black dash lines, while the H-bond interactions are indicated by blue continuous lines. (For interpretation of the references to colour in this figure legend, the reader is referred to the web version of this article.)

Table 4
Predicted binding affinities (AutoDock Vina score; kcal/mol) and the detailed interactions established upon docking of the ten selected allyl rhodanine-based derivatives, the docking control ligand ((hydroxyethyloxy)tri(ethyloxy)octane), AA, and baicalein against the *e*nzyme.

Scaffold series	Substituents (Ar)	Name	Vina score[1] (kcal/Mol)	Interactions	
				Hydrophobic residues	H-bond and other residues
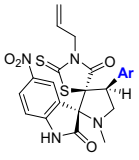	4-me-C_6H_4	**5a**	−8.633	Ala188, Phe192, Leu420, Val426, Ala606	Gln425(2)[2]
	4-OMe-C_6H_4	**5b**	−8.315	Tyr185, Phe192 (2)[2], Leu420, Leu605	Gln425(2)[2]
	4-cl-C_6H_4	**5c**	−8.362	Phe192, Leu420, Val426, Ala606	Gln425(2)[2]
	2-pyridyl	**5d**	−7.022	Phe192(3)[2], Leu419(2)[2]	–
	2-furyl	**5e**	−7.932	Phe192 (3)[2], Leu420	Gln425(2)[2]
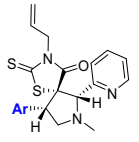	4-me-C_6H_4	**7a**	−7.227	Phe192(3)[2], Leu605, Leu610	πS^3: Phe184
	4-OMe-C_6H_4	**7b**	−7.084	Phe192, Leu419, Leu609, Leu610	Arg429
	4-cl-C_6H_4	**7c**	−7.619	Phe184, Ala188, Phe192, Leu415, Ala416, Leu420, Leu605, Leu610	–
	2-pyridyl	**7d**	−7.371	Phe184, Phe192(2)[2], Leu419(2)[2]	Arg429
	2-furyl	**7e**	−7.634	Phe184, Phe192, Leu420, Leu605(2)[2], Leu609, Leu610	–
Docking control ligand (hydroxyethyloxy) tri(ethyloxy)octane			−5.729	Phe365, Glu369(2)[2], Leu420, Val426, Thr431, Phe438, Val603, Ala606, Leu607	Glu369, Ala606
AA			−7.399	Phe184, Phe365, Glu369, Leu374, Ile412, Leu415, Ala416, Leu420, Val427, Thr431, Phe438, Val603, Leu607	–
Baicalein			−8.482	Phe184, Ile412, Leu415, Leu419, Leu420, Ala606, Leu610	Gln425(2)[2], Arg429, Asp602

[1] AutoDock Vina score (predicted affinity). [2] Multiple interactions. [3] π-Stacking interactions.

baicalein. Fig. S63 in the Supporting Information presents the root-mean-square fluctuation (RMSF) profiles for all *h*15-LOX-2–ligand complexes, enabling a comparative assessment of residue-level flexibility across the series. Table 5 summarizes the RMSF values specifically within the binding-site for each complex, highlighting how different ligands modulate local dynamics and pocket rigidity.

Local flexibility analysis based on RMSF shows that baicalein and compound **5c** markedly rigidify the *h*15-LOX-2 binding pocket, exhibiting low mean RMSF values over the binding-site residues (Table 5) of 0.53 Å and 0.47 Å, respectively. These values contrast with the higher average RMSF observed for compound **7b** (0.65 Å), highlighting the more compact and structurally constrained active-site architecture induced by baicalein and **5c**. This rigidification is further supported by the reduced variation in radius of gyration (Rg) observed for these

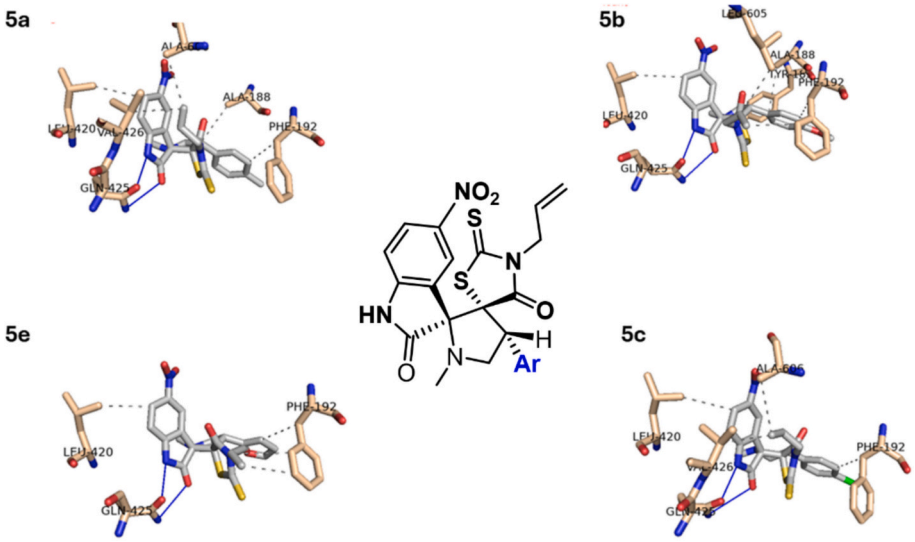

Fig. 4. Interaction profiles of the best-docked poses for compounds **5a, 5b, 5c and 5e**. Black dashed lines indicate hydrophobic interactions and blue continuous lines indicate H-bond interactions. (For interpretation of the references to colour in this figure legend, the reader is referred to the web version of this article.)

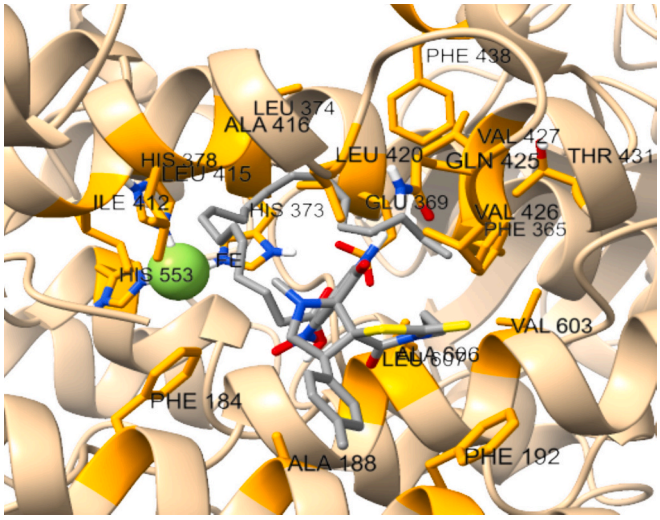

Fig. 5. Schematic representations of *h*15-LOX-2 overall structure and the active site's cavity, which is highlighted in orange. The catalytic iron is represented by a green sphere. The residues that coordinate Fe^{3+} (His373, His378, His553) and the residues of the active site's cavity are also shown. The interaction profile of the best-docked pose for the AA and derivative **5a** against the *h*15-LOX-2 enzyme. (For interpretation of the references to colour in this figure legend, the reader is referred to the web version of this article.)

complexes, with values of 0.41 Å for compound **5c** and 0.39 Å for baicalein, compared with 0.50 Å for **7b**, indicating a more compact and conformationally constrained global fold. Compound **5b** induces an intermediate effect, stabilizing most residues while allowing localized flexibility in specific loop regions. In contrast, compounds **5a** and **7b** increase the mobility of key active-site residues, generating a more dynamic ("breathing") binding pocket that samples a broader conformational space (with **7b** generally showing the highest flexibility overall across the binding-site residues listed). Global structural behavior assessed through root-mean-square deviation (RMSD) further reinforces these distinctions. Baicalein, despite rigidifying the pocket, allows the protein to explore two distinct global conformational substates, as evidenced by its broader and bimodal RMSD distribution (1.0–1.6 Å, see Fig. S64 in the Supporting Information). This suggests that baicalein induces local stabilization while permitting larger-scale rearrangements of the protein scaffold. Compound **5a** maintains a single, moderately flexible conformational state, with RMSD values confined to a narrower range (0.9–1.3 Å), indicating a globally stable but locally more dynamic complex. Compound **5c** produces the most rigid and conformationally homogeneous complex: after an initial equilibration phase, its RMSD remains tightly clustered around 1.0–1.3 Å with no evidence of multiple conformational basins. These observations align with its low RMSF values and its role as the strongest pocket-rigidifying ligand in the series. Together, RMSF, Rg and RMSD analyses demonstrate that local pocket rigidity and global conformational homogeneity act synergistically to define the structural impact of each inhibitor. These mechanistic differences may contribute to the cytotoxicity profiles observed across the A2780, A549 MDA-MB-231 and NCI-N592 cancer cell lines (see Table 2). Compound **5c**, the most rigidifying analogue, displays strong activity in both MDA-MB-231 (IC_{50} = 17.4 μM) and NCI-N592 (IC_{50} = 17.9 μM, $p < 0.01$) cells, which is compatible with a binding mode that enforces a highly constrained and well-defined active-site geometry. The activity of **5c** in NCI-N592, the only compound reaching a pharmacologically significant IC_{50} in this small-cell lung cancer model, further supports the link between pocket rigidification and effective enzyme inhibition. Compound **5b**, which induces moderate flexibility, shows the highest potency in A549 cells, suggesting that partial pocket adaptability may be advantageous in this cellular context. In contrast, compounds **5a** and **7b**, which generate the highest local mobility in the binding site, exhibit more pronounced cell-line selectivity: **5a** is most effective in A2780 cells (IC_{50} = 11.4 μM), while **7b** shows preferential activity in A549 cells relative to a more reduced activity in other cell lines. This pattern suggests that ligands inducing intermediate-to-high pocket rigidity (baicalein, **5c**) tend to promote a well-defined binding-site geometry but do not necessarily translate into uniformly higher cytotoxicity across cell lines, whereas ligands associated with higher binding-site flexibility (**5a**, **7b**) support more selective, context-dependent activity. None of the compounds reached a pharmacologically significant IC_{50} in the A431 epidermoid carcinoma cell line, consistent with the well-documented chemoresistance of this tumor model and suggesting that *h*15-LOX-2 inhibition alone may be insufficient to overcome A431-specific resistance mechanisms. MD-derived pocket dynamics provide a mechanistic rationale for the cell-line–dependent cytotoxicity trends, with rigidifying ligands (*e.g.*, **5c**/baicalein) favoring a more constrained binding mode and more flexible ligands (**5a**/**7b**) supporting selective activity. Overall, the MD results provide a plausible structural hypothesis for differential cellular

Table 5
RMSF values for key binding-site residues of *h*15-LOX-2 in complexes with the four allyl rhodanine-based derivatives (**5a–c** and **7b**) and the reference inhibitor baicalein. Residues are grouped into three binding-site regions ([184–192], [412–429] and [602–610]).

Compounds	RMSF (Å)														
	[184–192]				[412–429]							[602–610]			
	Phe184	Tyr185	Ala188	Phe192	Ile412	Leu415	Ala416	Leu419	Leu420	Gln425	Val426	Arg429	Asp602	Leu605	Ala606	Leu609	Leu610
5a	0.81	0.91	0.80	0.77	0.48	0.53	0.61	0.77	0.74	0.56	0.49	0.51	0.48	0.49	0.50	0.62	0.61
5b	0.62	0.73	0.59	0.49	0.51	0.56	0.51	0.77	0.51	0.55	0.50	0.54	0.43	0.45	0.45	0.48	0.49
5c	0.53	0.57	0.52	0.54	0.44	0.47	0.44	0.51	0.46	0.49	0.45	0.48	0.42	0.48	0.45	0.43	0.40
7b	0.81	0.93	0.76	0.75	0.54	0.63	0.59	0.83	0.77	0.58	0.54	0.57	0.48	0.49	0.56	0.66	0.64
Baicalein	0.60	0.65	0.62	0.63	0.46	0.54	0.54	0.58	0.55	0.62	0.49	0.52	0.44	0.45	0.44	0.48	0.46

responses, while acknowledging that cellular potency is also influenced by intracellular accumulation, metabolism, and potential off-target effects.

Although the MTT assay is a cell-based viability/proliferation readout and does not directly demonstrate target engagement [49], and docking/MD simulations do not directly quantify cellular potency, these approaches are complementary and together may provide a useful mechanistic framework for interpreting the biological results. In particular, compounds that induce a more rigid and conformationally stable *h*15-LOX-2 binding pocket (*e.g.*, **5c** and, to a lesser extent, **5b**) display more defined interaction profiles and sustained protein–ligand contacts throughout the simulations, which may favor effective enzyme inhibition. This behavior is compatible with their observed cytotoxic effects in specific cancer cell lines. Conversely, compounds associated with increased binding-site flexibility (*e.g.*, **5a** and **7b**) show more variable interaction patterns and correspondingly more cell line-dependent antiproliferative activity. Notably, **7b** combines potent activity in A549 cells with a weaker *h*15-LOX-2 computational signature, suggesting that additional targets and/or cellular mechanisms may contribute to its cytotoxicity. The generally weaker antiproliferative effects observed for the remaining series-**7** derivatives (**7a** and **7c–e**) are broadly consistent with their less favorable docking scores, while deviations from a strict potency–score relationship are expected in cell-based assays due to factors such as intracellular exposure and solubility.

These observations are in agreement with previous studies showing that stable protein–ligand interactions and reduced conformational fluctuations are often correlated with improved inhibitory potency, whereas increased flexibility may enable alternative binding modes or target promiscuity [50–53]. Therefore, while the computational results do not directly quantify biological activity, they provide a structural and dynamic rationale that supports and helps interpret the trends observed in the MTT assay [54].

Interestingly, the allyl rhodanine derivatives show improved cytotoxicity over baicalein in the three reference cell lines for which comparative data are available (IC_{50}: 46.23 μM in A2780, 20 μM in A549, 44 μM in MDA-MB-231) [42–44], with compounds **5a–c** exhibiting ~4-, 2-, and 2.5-fold higher potency across the respective cell lines. Notably, **5c** outperforms baicalein in MDA-MB-231 despite comparable pocket rigidification (RMSF: 0.47 *vs* 0.53 Å), indicating additional scaffold-driven effects. The activity of **5c** in NCI-N592 small-cell lung cancer cells (IC_{50} = 17.9 μM) extends the therapeutic relevance of this scaffold to a clinically challenging tumor type and supports further investigation in SCLC models. Overall, the results support these derivatives as promising *h*15-LOX-2 inhibitors with enhanced antiproliferative activity. These improvements may reflect the enhanced three-dimensionality of the spiro scaffold and the additional pharmacophoric features introduced by the isatinyl (series **5**) and pyridyl (series **7**) moieties, which are absent in the flavonoid core of baicalein.

2.7. Structure–activity relationship (SAR) studies

There is, in general, consistency between the experimental antiproliferative activity of compounds against the A2780, A549, MDA-MB-231, NCI-N592, and A431 cancer lines (see Tables 1 and 2) and the predicted binding to the *h*15-LOX-2 enzyme, as inferred by molecular docking of the allyl rhodanine-based derivatives and precursors (see Table 4 and Table S1 in the Supplementary Material). This relationship is consistent with previous reports describing rhodanine-based scaffolds as versatile modulators of biologically relevant targets [12,13], including enzymes of the pentose phosphate pathway (*e.g.*, G6PD and 6PGD), protein tyrosine phosphatases such as PTP1B, LAR, and TCPTP, anti-apoptotic Bcl-2 family proteins (Bcl-2, Bcl-xL, Mcl-1), and the JNK-stimulating phosphatase-1 (JSP-1). These diverse activities highlight the pharmacological relevance of the rhodanine core and support its use in the design of multifunctional anticancer agents. The subsequent molecular dynamics (MD) simulations performed on the most promising

candidates further refined this structure–activity relationship by revealing how each ligand modulates the conformational behavior and stability of the *h*15-LOX-2 active site, a mechanistic aspect also highlighted in structural studies of lipoxygenases [27]. The most active compounds belong to series **5** and **7**, and their chemical features are summarized in Fig. 6. MD analysis demonstrated that derivatives from series **5**, particularly **5c** (and to a lesser extent **5b**), induce pronounced rigidification of the *h*15-LOX-2 binding pocket, as reflected by their low RMSF values and reduced Rg variation. These ligands also maintain relatively narrow, unimodal RMSD distributions, indicating globally stable and conformationally homogeneous complexes. This dynamic stabilization may suggest sustained protein–ligand interactions within the *h15*-LOX-2 catalytic site and provides mechanistic insight into the strong antiproliferative effects observed for **5b** and **5c** (Table 1) and their IC_{50} values in selected cell lines (Table 2), while highlighting the pronounced cell-line dependence of activity (*e.g.*, **5c** is inactive in A549 at the IC_{50} level). Importantly, **5c** is also the only compound that reaches a pharmacologically significant IC_{50} in NCI-N592 small-cell lung cancer cells (17.9 μM), a result that is fully consistent with the highly rigid and conformationally homogeneous binding mode revealed by MD simulations and reinforces the SAR link between pocket rigidification and effective *h*15-LOX-2 inhibition. This selectivity, despite favorable binding-site dynamics, underscores that factors beyond target engagement, such as differential *h*15-LOX-2 expression, cellular permeability, or efflux mechanisms, modulate compound efficacy across cancer cell types. This is in agreement with the well-established ability of spirooxindole and rhodanine frameworks to promote tight and persistent protein–ligand interactions [13,22].

Among the series-**5** derivatives not subjected to MD simulations, compound **5e** shows a favorable docking score and relevant antiproliferative activity in A2780 and A549 cells, while being borderline in MDA-MB-231 (Table 2). On the other hand, compound **5d** exhibited a less favorable docking score, consistent with its moderate antiproliferative activity limited to A2780 (Table 2).

The allyl rhodanine–spiro pyrrolidine scaffold (highlighted in blue in Fig. 6) appears to be essential for both antiproliferative activity and predicted *h*15-LOX-2 binding. Within this framework, the isatinyl moiety present in series **5** (highlighted in pink) plays a key role in enhancing binding stability, as supported by the reduced flexibility of key active site residues and the compact global fold observed during MD simulations. This is consistent with the recognized role of spirooxindoles as rigid, three-dimensional pharmacophores that enhance shape complementarity and binding persistence [55]. An exception to this trend is compound **7b**, which shows potent activity in the A549 cell line despite exhibiting lower predicted affinity for *h*15-LOX-2 and higher flexibility in MD simulations, including broader RMSD distributions and elevated RMSF values. This discrepancy suggests that **7b** may exert its cytotoxic effects through alternative molecular targets or mechanisms not captured by the docking and MD models. Differences in cellular uptake, metabolism, or context-dependent signaling pathways may also contribute to its selective activity. Further studies will be required to elucidate the molecular basis of its behavior. Overall, the integration of docking, MD simulations, and biological evaluation provides a coherent SAR framework in which ligands that rigidify the *h*15-LOX-2 pocket tend to favor a more well-defined binding geometry and may contribute to antiproliferative activity in specific cellular contexts, whereas ligands that increase pocket flexibility display more variable, cell-line-dependent effects.

2.8. Physicochemical, pharmacokinetic, and in-silico toxicity prediction

The physicochemical, pharmacokinetic, and toxicity properties of the most active allyl-rhodanine derivatives (**5a–c** and **7b**) were assessed using the Deep-PK web server [56,57]. The predicted parameters are summarized in Table 6.

All derivatives exhibited $logD_{7.4}$ values >3, indicating relatively high lipophilicity, which may favor membrane permeability but could limit aqueous solubility. In line with Lipinski's rule of five, logP values remained below 5; within the series, **7b** showed improved solubility (logS = −3.59 *vs* < −4 for **5a–c**), suggesting a more favorable developability profile [57].

Caco-2 permeability values indicated low intestinal permeability across all compounds. Nevertheless, **5a**, **5c**, and **7b** were classified as orally bioavailable and systemically absorbed, whereas **5b** was considered absorbed but not orally bioavailable, suggesting reduced effective exposure. All compounds showed low skin permeability.

All derivatives were predicted to cross the blood–brain barrier (BBB-penetrable), suggesting potential central nervous system exposure. Compound **7b** showed the lowest predicted plasma protein binding, indicating a higher free fraction in circulation as output by Deep-PK model ([57]; values >100 reflect model-specific scaling). A moderate steady-state volume of distribution (SSVD) was predicted for all four derivatives.

Regarding metabolism, none of the derivatives showed relevant inhibition of the hepatic uptake transporters OATP1B1 and OATP1B3, which play key roles in the uptake of xenobiotics into hepatocytes. In contrast, all compounds were predicted to inhibit the major hepatic drug-metabolizing enzymes CYP2C19, CYP2C9, CYP2D6, and CYP3A4, indicating a potential risk of cytochrome P450–mediated drug–drug interactions. Notably, derivative **5b** was the only compound identified as a non-inhibitor of CYP1A2. Substrate behavior varied across the series: **5b** and **7b** were substrates of multiple CYP isoforms, **5a** showed

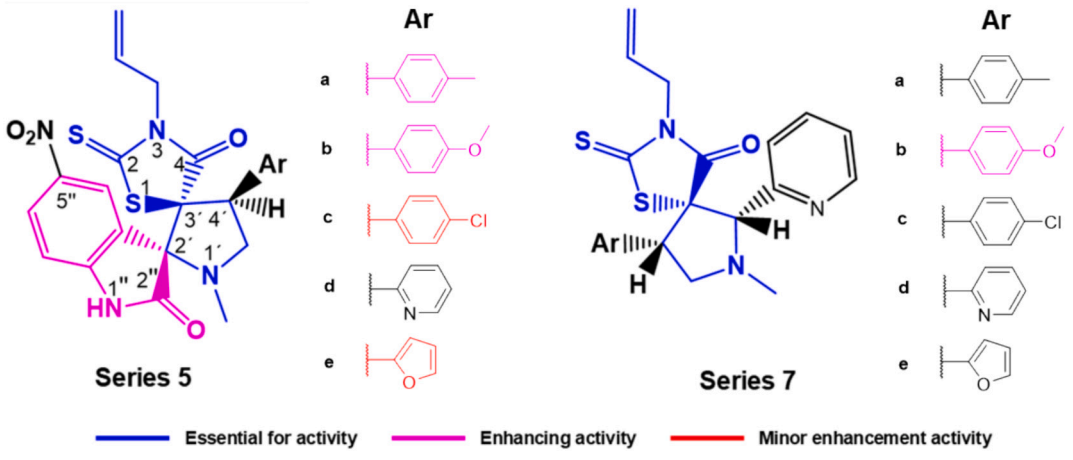

Fig. 6. Chemical structures and SAR analysis of ten derivatives from series **5** and **7**.

Table 6
Predicted ADME/Tox profiling of four selected allyl-rhodanine derivatives (Deep-PK).

Properties	ADME/tox	Allyl-rhodanine derivatives			
		5a	5b	5c	7b
Physicochemical	Log $D_{7.4}$	3.780	3.500	3.980	3.320
	Log P	3.510	3.080	3.820	2.740
	Log S	−4.810	−4.670	−4.750	−3.590
Absorption	Caco-2 permeability[a]	−5.170	−5.280	−5.280	−4.640
	Human Oral bioavailability 20%	Bioavailable	Non-bioavailable	Bioavailable	
	Human intestinal absorption	Absorbed			
	Skin permeability	Low			
	Blood-brain barrier	Penetrable			
Distribution	Plasma protein binding	103.410	100.510	102.150	79.100
	SSVD[b]	1.420	1.460	1.570	0.860
	CYP 1A2 inhibitor	Inhibitor	Non-inhibitor	Inhibitor	
	CYP 2C19, CYP 2C9, CYP 2D6, CYP 3A4 inhibitor	Inhibitor			
	OATP1B1, OATP1B3 inhibitor	Non-inhibitor			
Metabolism	CYP 1A2, CYP 2D6 substrate	Non-substrate			
	CYP 2C19 substrate	Substrate	Substrate	Non-substrate	Substrate
	CYP 2C9 substrate	Non-substrate			Substrate
	CYP 3A4 substrate	Non-substrate	Substrate	Non-substrate	Substrate
Excretion	Clearance	9.650	8.900	8.110	9.200
	Organic cation transporter 2	Non-inhibitor			
Toxicity	AMES mutagenesis	Toxic			Safe
	Avian	Safe			
	Bee	Toxic			
	Biodegradation	Safe			
	Carcinogenesis	Safe			
	Crustacean	Toxic			
	Liver injury I	Toxic			
	Eye corrosion	Safe			
	Eye irritation	Safe			
	Maximum tolerated dose	0.480	0.560	0.410	0.500
	Liver injury II	Toxic			
	hERG blocker	Safe			
	Skin sensitization	Safe			Toxic

[a] Caco-2 permeability values are reported as provided by Deep PK (https://biosig.lab.uq.edu.au/deeppk/theory). [b] Steady-state volume of distribution.

limited liability, whereas **5c** was not identified as a CYP substrate [57].

In toxicity assessment, only **7b** was free of AMES mutagenicity alerts, whereas the remaining derivatives **5a–c** showed potential mutagenic risk. All compounds were predicted to be non-carcinogenic. While **5a–c** were non-sensitizing, **7b** showed potential skin sensitization risk. Regarding systemic toxicity, **5a**, **5b**, and **7b** exhibited relatively higher maximum tolerated dose (MTD) values, whereas **5c** showed a lower tolerated dose [57].

Overall, the series shows a mixed ADMET profile with clear structure-dependent differences. Compound **7b** displays the most balanced overall profile, combining improved solubility, reduced plasma protein binding, and absence of mutagenicity alerts, although liabilities such as CYP inhibition and potential sensitization remain. Other derivatives exhibit specific advantages in individual parameters, particularly **5c** in metabolic liability and **5b** in CYP1A2 and substrate behavior, highlighting the impact of structural variation on ADMET properties. Collectively, these findings identify **7b** as the most balanced lead from a developability perspective, while **5c** emerges as the most potent but pharmacokinetically more challenging candidate, providing a clear indication for future design efforts.

3. Conclusions

This work presents new insights and advancements in the synthesis and anticancer activity of dispiro-indole-pyrrolidine-rhodanine and spiropyrrolidine-rhodanine derivatives bearing an *N*-allyl moiety on the rhodanine unit. The study demonstrated that *N*-allyl-5-arylidene-rhodanine derivatives undergo 1,3-dipolar cycloaddition with azomethine ylides (generated from sarcosine and either 5-nitroisatin or 2-pyridinecarboxaldehyde) with high site- and regioselectivity at the double bond conjugated to the rhodanine moiety. Dispiro-indole derivatives (series **5**) were obtained in moderate yields ranging from 50 to 66%, likely due to steric hindrance, while pyridyl-substituted spiro compounds (series **7**) showed higher yields of 64 to 77%.

In vitro testing against A2780, A549, MDA-MB-231, NCI-N592, and A431 cell lines revealed notable antiproliferative activity, particularly for several compounds from series **5**, with **5b** and **7b** exhibiting strong antiproliferative and apoptotic effects against A549 cells. Notably, **5c** emerged as the only derivative active against the chemoresistant NCI-N592 small-cell lung cancer line, while none of the compounds showed significant activity in A431 epidermoid carcinoma cells, suggesting selectivity towards specific tumor contexts. Molecular docking studies targeting *h*15-LOX-2, with baicalein as a reference inhibitor, supported these findings and provided a preliminary structure–activity rationale. Importantly, molecular dynamics simulations refined and strengthened the SAR by revealing how each ligand modulates the conformational landscape of *h*15-LOX-2. Compounds **5b** and **5c**, which showed potent biological activity, also induced marked rigidification of the binding pocket, characterized by low RMSF values, reduced Rg variation, and narrow unimodal RMSD distributions. These features indicate globally stable and conformationally homogeneous complexes, compatible with more persistent binding. In contrast, compound **7b**, despite its potent activity in A549 cells, displayed higher flexibility in MD simulations, suggesting that its cytotoxic effects may involve additional molecular targets or context-dependent mechanisms beyond *h*15-LOX-2 inhibition. Complementary *in silico* ADMET predictions identified **7b** as the lead with the most favorable developability profile, while **5c** emerged as the most potent but pharmacokinetically more challenging candidate, highlighting structure-dependent liabilities that will guide subsequent optimization. These results highlight the synthetic versatility and promising anticancer potential of *N*-allyl-rhodanine spiro derivatives, supporting further investigation as lead compounds for therapeutic development.

4. Experimental

4.1. Physical measurements

All compounds were characterized using standard techniques. Chromatographic separations were performed on silica gel by column chromatography or TLC. Full details of all physical measurements are provided in the Supporting Information.

4.2. Experimental protocols

Detailed synthetic procedures, compound characterization data, X-ray diffraction experiments, biological assays (MTT assay, cell culture), molecular docking and molecular dynamics studies, and ADMET (Absorption, Distribution, Metabolism, Excretion, and Toxicity) predictions are described in the Supporting Information.

Funding and acknowledgements

The authors thank to the University of Aveiro and FCT/MCTES for the financial support of the UID/50006/2025 (DOI: 10.54499/UID/50006/2025) - Laboratório Associado para a Química Verde - Tecnologias e Processos Limpos. This work was developed within the scope of the project CICECO – Aveiro Institute of Materials, UID/50011 & LA/P/0006/2020 (DOI 10.54499/LA/P/0006/2020), financed by national funds through the FCT/MCTES (PIDDAC). Thanks are also due to the Erasmus+ program which allows student exchange. The authors also acknowledge the support from Italian Ministry of Health, Italy, under grant "Ricerca Corrente", 2024. Florbela Pereira gratefully acknowledges FCT, I.P., through the CEEC-Individual Program (CEECIND/01649/2021).

CRediT authorship contribution statement

Redouane Er-raqioui: Investigation. **José A.S. Cavaleiro:** Writing – review & editing, Validation. **M. Amparo F. Faustino:** Writing – review & editing, Validation. **Filipe A. Almeida Paz:** Writing – original draft, Formal analysis. **Maurizio Viale:** Writing – original draft, Investigation, Formal analysis. **Fabrizio Loiacono:** Investigation, Resources, Writing – review & editing. **El Mostapha Rakib:** Writing – review & editing, Supervision, Conceptualization. **Maria da Graça P.M.S. Neves:** Writing – review & editing, Validation. **Florbela Pereira:** Writing – review & editing, Writing – original draft, Methodology, Investigation. **Nuno M. M. Moura:** Writing – review & editing, Writing – original draft, Supervision, Methodology, Conceptualization.

Declaration of competing interest

The authors declare that they have no known competing financial interests or personal relationships that could have appeared to influence the work reported in this paper.

Appendix A. Supplementary data

Supplementary data to this article can be found online at https://doi.org/10.1016/j.bioorg.2026.110154.

Data availability

Data will be made available on request.

References

[1] S. Kaur Manjal, R. Kaur, R. Bhatia, K. Kumar, V. Singh, R. Shankar, R. Kaur, R. K. Rawal, Synthetic and medicinal perspective of thiazolidinones: a review, Bioorg. Chem. 75 (2017) 406–423, https://doi.org/10.1016/j.bioorg.2017.10.014.

[2] A.K.D. Bin Ahmad Kamar, L. Ju Yin, C. Tze Liang, G. Tjin Fung, V.R. Avupati, Rhodanine scaffold: a review of antidiabetic potential and structure–activity relationships (SAR), Med. Drug Discov. 15 (2022) 100131, https://doi.org/10.1016/j.medidd.2022.100131.

[3] S.M. Mousavi, M. Zarei, S.A. Hashemi, A. Babapoor, A.M. Amani, A conceptual review of rhodanine: current applications of antiviral drugs, anticancer and antimicrobial activities, Artif. Cells, Nanomedicine, Biotechnol. 47 (2019) 1132–1148, https://doi.org/10.1080/21691401.2019.1573824.

[4] L. Zhu, C. Ye, S. Chen, Y. Fang, Y. Zhang, T. Zhang, Rhodanine derivatives containing 5-Aryloxypyrazole moiety as anti-inflammatory and anticancer agents, Chem. Biodivers. 21 (2024), https://doi.org/10.1002/cbdv.202301844.

[5] M. Krátký, J. Vinšová, J. Stolaříková, Antimicrobial activity of rhodanine-3-acetic acid derivatives, Bioorg. Med. Chem. 25 (2017) 1839–1845, https://doi.org/10.1016/j.bmc.2017.01.045.

[6] K. Pudhom, K. Kasai, H. Terauchi, H. Inoue, M. Kaiser, R. Brun, M. Ihara, K. Takasu, Synthesis of three classes of rhodacyanine dyes and evaluation of their in vitro and in vivo antimalarial activity, Bioorg. Med. Chem. 14 (2006) 8550–8563, https://doi.org/10.1016/j.bmc.2006.08.035.

[7] M. Sortino, P. Delgado, S. Juárez, J. Quiroga, R. Aboníа, B. Insuasty, M. Nogueras, L. Rodero, F.M. Garibotto, R.D. Enriz, Synthesis and antifungal activity of (Z)-5-arylidenerhodanines, Bioorg. Med. Chem. 15 (2007) 484–494, https://doi.org/10.1016/j.bmc.2006.09.038.

[8] C. Tintori, G. Iovenitti, E.R. Ceresola, R. Ferrarese, C. Zamperini, A. Brai, G. Poli, E. Dreassi, V. Cagno, D. Lembo, F. Canducci, M. Botta, Rhodanine derivatives as potent anti-HIV and anti-HSV microbicides, PloS One 13 (2018) e0198478, https://doi.org/10.1371/journal.pone.0198478.

[9] N. Siddiqui, S. Andalip, R. Bawa, O. Afzal Ali, Mj Akhtar, B. Azad, R. Kumar, Antidepressant potential of nitrogen-containing heterocyclic moieties: an updated review, J. Pharm. Bioallied Sci. 3 (2011) 194, https://doi.org/10.4103/0975-7406.80765.

[10] I.H. Hiba, J.K. Koh, C.W. Lai, S.M. Mousavi, I.A. Badruddin, M. Hussien, J.P. Wong, Polyrhodanine-based nanomaterials for biomedical applications: a review, Heliyon 10 (2024) e28902, https://doi.org/10.1016/j.heliyon.2024.e28902.

[11] A. Sharma, D. Sharma, N. Saini, S.V. Sharma, V.K. Thakur, R.K. Goyal, P. C. Sharma, Recent advances in synthetic strategies and SAR of thiazolidin-4-one containing molecules in cancer therapeutics, Cancer Metastasis Rev. 42 (2023) 847–889, https://doi.org/10.1007/s10555-023-10106-1.

[12] J. Szczepański, H. Tuszewska, N. Trotsko, Anticancer Profile of Rhodanines: Structure–Activity Relationship (SAR) and Molecular Targets—A Review, Molecules 27 (2022) 3750, https://doi.org/10.3390/molecules27123750.

[13] L.J. Yin, A.K.D. Bin Ahmad Kamar, G.T. Fung, C.T. Liang, V.R. Avupati, Review of anticancer potentials and structure-activity relationships (SAR) of rhodanine derivatives, Biomed. Pharmacother. 145 (2022) 112406, https://doi.org/10.1016/j.biopha.2021.112406.

[14] A.L. Cardoso, M.I.L. Soares, 1,3-dipolar cycloadditions involving allenes: synthesis of five-membered rings, Curr. Org. Chem. 23 (2020) 3064–3134, https://doi.org/10.2174/1385272823666191203122959.

[15] S. Pookkandam Parambil, S. Pulikkal Veettil, W. Dehaen, The synthesis of five-membered N-heterocycles by cycloaddition of nitroalkenes with (in)organic Azides and other 1,3-dipoles, Synthesis (Stuttg). 54 (2022) 910–924, https://doi.org/10.1055/a-1547-0196.

[16] A. Linden, E.M.A.H. Awad, H. Heimgartner, A rhodanine derivative and its cycloadduct with diphenyl nitrile imine, acta Crystallogr, Sect. C Cryst. Struct. Commun. 55 (1999) 1877–1881, https://doi.org/10.1107/S0108270199008975.

[17] R. Murugan, S. Anbazhagan, S. Sriman Narayanan, Synthesis and in vivo antidiabetic activity of novel dispiropyrrolidines through [3+2] cycloaddition reactions with thiazolidinedione and rhodanine derivatives, Eur. J. Med. Chem. 44 (2009) 3272–3279, https://doi.org/10.1016/j.ejmech.2009.03.035.

[18] S.V. Kurbatov, V.V. Zarubaev, L.A. Karpinskaya, A.A. Shvets, M.E. Kletsky, O. N. Burov, P.G. Morozov, O.I. Kiselev, V.I. Minkin, Synthesis and antiviral activity of bis-spirocyclic derivatives of rhodanine, Russ. Chem. Bull. 63 (2014) 1130–1136, https://doi.org/10.1007/s11172-014-0560-4.

[19] S. Ponnuchamy, R.V. Sumesh, R. Ranjith Kumar, Regioselective synthesis of novel dispiro oxindole–pyrrolizine–thiazolidine-2,4-dione hybrids, Tetrahedron Lett. 56 (2015) 4374–4376, https://doi.org/10.1016/j.tetlet.2015.05.090.

[20] A. Toumi, S. Boudriga, K. Hamden, M. Sobeh, M. Cheurfa, M. Askri, M. Knorr, C. Strohmann, L. Brieger, Synthesis, antidiabetic activity and molecular docking study of rhodanine-substitued spirooxindole pyrrolidine derivatives as novel α-amylase inhibitors, Bioorg. Chem. 106 (2021) 104507, https://doi.org/10.1016/j.bioorg.2020.104507.

[21] S. Lanka, S. Thennarasu, P.T. Perumal, Stoichiometry-controlled cycloaddition of azomethine ylide with dipolarophiles: chemoselective and regioselective synthesis of bis- and tris-spirooxindole derivatives, Tetrahedron Lett. 55 (2014) 2585–2588, https://doi.org/10.1016/j.tetlet.2014.02.121.

[22] M.S. Nafie, I. Shawish, S.A. Fahmy, M.K. Diab, M.M. Abdelfattah, B.M. Hassen, K. M. Darwish, A. El-Faham, A. Barakat, Recent advances in the halogenated spirooxindoles as novel anticancer scaffolds: chemistry and bioactivity approach, RSC Adv. 15 (2025) 22336–22375, https://doi.org/10.1039/D5RA03404C.

[23] M.H. Helal, M.E. Owda, A.T. Mogharbel, A. Hamzah Alessa, N. Omer, M. A. Abdelaziz, I. Ibrahim, E.M. Eliwa, C3-Spirooxindoles: divergent chemical synthesis and bioactivities (2018–2023), Bioorg. Chem. 143 (2024) 107091, https://doi.org/10.1016/j.bioorg.2023.107091.

[24] S.S. Panda, A.S. Girgis, M.N. Aziz, M.S. Bekheit, Spirooxindole: a versatile biologically active heterocyclic scaffold, Molecules 28 (2023) 618, https://doi.org/10.3390/molecules28020618.

[25] Y.-T. Yang, J.-F. Zhu, G. Liao, H.-J. Xu, B. Yu, The development of biologically important Spirooxindoles as new antimicrobial agents, Curr. Med. Chem. 25 (2018) 2233–2244, https://doi.org/10.2174/0929867325666171129131311.
[26] B. Yu, D.-Q. Yu, H.-M. Liu, Spirooxindoles: promising scaffolds for anticancer agents, Eur. J. Med. Chem. 97 (2015) 673–698, https://doi.org/10.1016/j.ejmech.2014.06.056.
[27] H. Kuhn, S. Banthiya, K. van Leyen, Mammalian lipoxygenases and their biological relevance, Biochim. Biophys. Acta - Mol. Cell Biol. Lipids. 1851 (2015) 308–330, https://doi.org/10.1016/j.bbalip.2014.10.002.
[28] C. Schneider, D.A. Pratt, N.A. Porter, A.R. Brash, Control of oxygenation in lipoxygenase and cyclooxygenase catalysis, Chem. Biol. 14 (2007) 473–488, https://doi.org/10.1016/j.chembiol.2007.04.007.
[29] I. Daurkin, E. Eruslanov, T. Stoffs, G.Q. Perrin, C. Algood, S.M. Gilbert, C.J. Rosser, L.-M. Su, J. Vieweg, S. Kusmartsev, Tumor-associated macrophages mediate immunosuppression in the renal Cancer microenvironment by activating the 15-Lipoxygenase-2 pathway, Cancer Res. 71 (2011) 6400–6409, https://doi.org/10.1158/0008-5472.CAN-11-1261.
[30] O.S. Afifi, O.G. Shaaban, H.A. Abd El Razik, S.E.-D.A. Shams El-Dine, F.A. Ashour, A.A. El-Tombary, M.M. Abu-Serie, Synthesis and biological evaluation of purine-pyrazole hybrids incorporating thiazole, thiazolidinone or rhodanine moiety as 15-LOX inhibitors endowed with anticancer and antioxidant potential, Bioorg. Chem. 87 (2019) 821–837, https://doi.org/10.1016/j.bioorg.2019.03.076.
[31] A. Starosotnikov, M. Bastrakov, Nitropyridines in the synthesis of bioactive molecules, Pharmaceuticals 18 (2025) 692, https://doi.org/10.3390/ph18050692.
[32] D. Sahu, P.S.R. Sreekanth, P.K. Behera, M.K. Pradhan, A. Patnaik, S. Salunkhe, R. Cep, Advances in synthesis, medicinal properties and biomedical applications of pyridine derivatives: a comprehensive review, Eur. J. Med. Chem. Reports. 12 (2024) 100210, https://doi.org/10.1016/j.ejmcr.2024.100210.
[33] M. Marinescu, C.-V. Popa, Pyridine compounds with antimicrobial and antiviral activities, Int. J. Mol. Sci. 23 (2022) 5659, https://doi.org/10.3390/ijms23105659.
[34] Y. Ling, Z.-Y. Hao, D. Liang, C.-L. Zhang, Y.-F. Liu, Y. Wang, The expanding role of pyridine and dihydropyridine scaffolds in drug design, Drug Des. Devel. Ther. 15 (2021) 4289–4338, https://doi.org/10.2147/DDDT.S329547.
[35] A.M. Starosotnikov, M.A. Bastrakov, Recent developments in the synthesis of HIV-1 integrase Strand transfer inhibitors incorporating pyridine moiety, Int. J. Mol. Sci. 24 (2023) 9314, https://doi.org/10.3390/ijms24119314.
[36] R. El Ajlaoui, A. Ouafa, S. Mojahidi, L. El Ammari, M. Saadi, E.M. Rakib, Unexpected synthesis of novel 3-Allyl-5-(arylidene)-2-thioxo-thiazolidin-4-ones in reactions of 3-Allylrhodanine with 2-Arylidene-4-methyl-5-oxopyrazolidinium ylides, Synth. Commun. 45 (2015) 2035–2042, https://doi.org/10.1080/00397911.2015.1063655.
[37] M. Duhan, R. Singh, M. Devi, J. Sindhu, P. Kumar, S. Kumar, R. Kataria, A. Kumar, S. Lal, D. Singh, Thiazolidine-2,4-dione framework containing spiropyrrolidine-oxindole and 1,2,3-triazole scaffold: synthesis, in vitro α-amylase inhibition and in silico studies, New J. Chem. 47 (2023) 5399–5412, https://doi.org/10.1039/D2NJ05059E.
[38] M. Ghandi, A. Taheri, A. Abbasi, Diastereoselective synthesis of nicotine derivatives via 1,3-dipolar cycloaddition reactions, J. Heterocyclic Chem. 47 (2010) 611–615, https://doi.org/10.1002/jhet.366.
[39] M. Puri, K. Gawri, R. Dawar, Therapeutic strategies for BRAF mutation in non-small cell lung cancer: a review, Front. Oncol. 13 (2023) 1141876, https://doi.org/10.3389/fonc.2023.1141876.
[40] M.J. Kobe, D.B. Neau, C.E. Mitchell, S.G. Bartlett, M.E. Newcomer, The structure of human 15-Lipoxygenase-2 with a substrate mimic, J. Biol. Chem. 289 (2014) 8562–8569, https://doi.org/10.1074/jbc.M113.543777.
[41] J.D. Deschamps, V.A. Kenyon, T.R. Holman, Baicalein is a potent in vitro inhibitor against both reticulocyte 15-human and platelet 12-human lipoxygenases, Bioorg. Med. Chem. 12 (2006) 4295–4301, https://doi.org/10.1016/j.bmc.2006.01.057.
[42] Q. Pan, M. Xue, S. Xiao, Y. Wan, D. Xu, A combination therapy with baicalein and Taxol promotes mitochondria-mediated cell apoptosis: involving in Akt/β-catenin Signaling pathway, DNA Cell Biol. 35 (2016) 646–656, https://doi.org/10.1089/dna.2016.3312.
[43] J. Li, D. Zhang, S. Wang, P. Yu, J. Sun, Y. Zhang, X. Meng, J. Li, L. Xiang, Baicalein induces apoptosis by inhibiting the glutamine-mTOR metabolic pathway in lung cancer, J. Adv. Res. 68 (2025) 341–357, https://doi.org/10.1016/j.jare.2024.02.023.
[44] A.Y. Al-Kabariti, M.A. Abbas, M. Alqaraleh, R. Madi, S.D. Shnyder, Baicalein sensitizes triple negative breast Cancer cells to cisplatin by activating apoptosis, Nat. Prod. Commun. 20 (2025) 1–12, https://doi.org/10.1177/1934578X251368753.
[45] L.G. Viviani, T.S. Iijima, E. Piccirillo, L. Rezende, T.G.P. Alegria, L.E.S. Netto, A. T. do Amaral, S. Miyamoto, Identification of novel human 15-Lipoxygenase-2 (h15-LOX-2) inhibitors using a virtual screening approach, J. Med. Chem. 68 (2025) 307–323, https://doi.org/10.1021/acs.jmedchem.4c01884.
[46] P. Eastman, J. Swails, J.D. Chodera, R.T. McGibbon, Y. Zhao, K.A. Beauchamp, L.-P. Wang, A.C. Simmonett, M.P. Harrigan, C.D. Stern, R.P. Wiewiora, B.R. Brooks, V.S. Pande, OpenMM 7: rapid development of high performance algorithms for molecular dynamics, PLoS Comput. Biol. 13 (2017) e1005659, https://doi.org/10.1371/journal.pcbi.1005659.
[47] Tamarind Bio, Computational tools for structural biology and molecular simulation, https://www.tamarind.bio/ (accessed March 2026).
[48] P.R. Arantes, M.D. Polêto, C. Pedebos, R. Ligabue-Braun, Making it rain: cloud-based molecular simulations for everyone, J. Chem. Inf. Model. 61 (2021) 4852–4856, https://doi.org/10.1021/acs.jcim.1c00998.
[49] T. Mosmann, Rapid colorimetric assay for cellular growth and survival: application to proliferation and cytotoxicity assays, J. Immunol. Methods 65 (1983) 55–63, https://doi.org/10.1016/0022-1759(83)90303-4.
[50] J.D. Durrant, J.A. McCammon, Molecular dynamics simulations and drug discovery, BMC Biol. 9 (2011) 71, https://doi.org/10.1186/1741-7007-9-71.
[51] K. Liu, H. Kokubo, Exploring the stability of ligand binding modes to proteins by molecular dynamics simulations: a cross-docking study, J. Chem. Inf. Model. 57 (2017) 2514–2522, https://doi.org/10.1021/acs.jcim.7b00412.
[52] P. Cozzini, G.E. Kellogg, F. Spyrakis, D.J. Abraham, G. Costantino, A. Emerson, F. Fanelli, H. Gohlke, L.A. Kuhn, G.M. Morris, M. Orozco, T.A. Pertinhez, M. Rizzi, C.A. Sotriffer, Target flexibility: an emerging consideration in drug discovery and design, J. Med. Chem. 51 (2008) 6237–6255, https://doi.org/10.1021/jm800562d.
[53] S.J. Teague, Implications of protein flexibility for drug discovery, Nat. Rev. Drug Discov. 2 (2003) 527–541, https://doi.org/10.1038/nrd1129.
[54] M. De Vivo, M. Masetti, G. Bottegoni, A. Cavalli, Role of molecular dynamics and related methods in drug discovery, J. Med. Chem. 59 (2016) 4035–4061, https://doi.org/10.1021/acs.jmedchem.5b01684.
[55] M.E. Welsch, S.A. Snyder, B.R. Stockwell, Privileged scaffolds for library design and drug discovery, Curr. Opin. Chem. Biol. 14 (2010) 347–361, https://doi.org/10.1016/j.cbpa.2010.02.018.
[56] Deep-PK web server, University of Queensland, https://biosig.lab.uq.edu.au/deeppk/ (accessed March 2026).
[57] Y. Myung, A.G.C. de Sá, D.B. Ascher, Deep-PK: deep learning for small molecule pharmacokinetic and toxicity prediction, Nucleic Acids Res. 52 (2024) W469–W475, https://doi.org/10.1093/nar/gkae254.